

University of Wollongong

## Research Online

---

Australian Institute for Innovative Materials -  
Papers

Australian Institute for Innovative Materials

---

1-1-2017

### Phosphorus-Based Alloy Materials for Advanced Potassium-Ion Battery Anode

Wenchao Zhang

*University of Wollongong, wz990@uowmail.edu.au*

Jianfeng Mao

*Chinese Academy Of Sciences, jmao@uow.edu.au*

Sean Li

*University of New South Wales, University of Queensland, sean.li@unsw.edu.au*

Zhixin Chen

*University of Wollongong, zchen@uow.edu.au*

Zaiping Guo

*University of Wollongong, zguo@uow.edu.au*

Follow this and additional works at: <https://ro.uow.edu.au/aiimpapers>



Part of the [Engineering Commons](#), and the [Physical Sciences and Mathematics Commons](#)

---

#### Recommended Citation

Zhang, Wenchao; Mao, Jianfeng; Li, Sean; Chen, Zhixin; and Guo, Zaiping, "Phosphorus-Based Alloy Materials for Advanced Potassium-Ion Battery Anode" (2017). *Australian Institute for Innovative Materials - Papers*. 2477.

<https://ro.uow.edu.au/aiimpapers/2477>

Research Online is the open access institutional repository for the University of Wollongong. For further information contact the UOW Library: [research-pubs@uow.edu.au](mailto:research-pubs@uow.edu.au)

---

## Phosphorus-Based Alloy Materials for Advanced Potassium-Ion Battery Anode

### Abstract

Potassium-ion batteries (PIBs) are interesting as one of the alternative metal-ion battery systems to lithium-ion batteries (LIBs) due to the abundance and low cost of potassium. We have herein investigated Sn<sub>4</sub>P<sub>3</sub>/C composite as a novel anode material for PIBs. The electrode delivered a reversible capacity of 384.8 mA h g<sup>-1</sup> at 50 mA g<sup>-1</sup> and a good rate capability of 221.9 mA h g<sup>-1</sup>, even at 1 A g<sup>-1</sup>. Its electrochemical performance is better than any anode material reported so far for PIBs. It was also found that the Sn<sub>4</sub>P<sub>3</sub>/C electrode displays a discharge potential plateau of 0.1 V in PIBs, slightly higher than for sodium-ion batteries (SIBs) (0.01 V), and well above the plating potential of metal. This diminishes the formation of dendrites during cycling, and thus Sn<sub>4</sub>P<sub>3</sub> is a relatively safe anode material, especially for application in large-scale energy storage, where large amounts of electrode materials are used. Furthermore, a possible reaction mechanism of the Sn<sub>4</sub>P<sub>3</sub>/C composite as PIB anode is proposed. This work may open up a new avenue for further development of alloy-based anodes with high capacity and long cycle life for PIBs.

### Disciplines

Engineering | Physical Sciences and Mathematics

### Publication Details

Zhang, W., Mao, J., Li, S., Chen, Z. & Guo, Z. (2017). Phosphorus-Based Alloy Materials for Advanced Potassium-Ion Battery Anode. *Journal of the American Chemical Society*, 139 (9), 3316-3319.

# Phosphorus-based alloy materials for advanced potassium-ion battery anode

Wenchao Zhang,<sup>a, b, ‡</sup> Jianfeng Mao,<sup>b, ‡</sup> Sean Li,<sup>c</sup> Zhixin Chen,<sup>a, \*</sup> Zaiping Guo<sup>a, b, \*</sup>

<sup>a</sup> Engineering Materials Institute, School of Mechanical, Materials & Mechatronics Engineering, University of Wollongong, NSW 2500, Australia.

<sup>b</sup> Institute for Superconducting & Electronic Materials, University of Wollongong, Wollongong, NSW 2522, Australia.

<sup>c</sup> School of Materials Science and Engineering, The University of New South Wales, NSW 2052, Australia.

## Supporting Information

**ABSTRACT:** Potassium-ion batteries (PIBs) are interesting as one of the alternative metal-ion battery systems to lithium-ion batteries (LIBs) due to the abundance and low cost of potassium. We have herein investigated Sn<sub>4</sub>P<sub>3</sub>/C composite as a novel anode material for PIBs. The electrode delivered a reversible capacity of 384.8 mA h g<sup>-1</sup> at 50 mA g<sup>-1</sup> and a good rate capability of 221.9 mA h g<sup>-1</sup>, even at 1 A g<sup>-1</sup>. Its electrochemical performance is better than any anode material reported so far for PIBs. It was also found that the Sn<sub>4</sub>P<sub>3</sub>/C electrode displays a discharge potential plateau of 0.1 V in PIBs, slightly higher than for sodium-ion batteries (0.01 V), and well above the plating potential of metal. This diminishes the formation of dendrites during cycling, and thus, Sn<sub>4</sub>P<sub>3</sub> is a relatively safe anode material, especially for application in large-scale energy storage, where large amounts of electrode materials are used. Furthermore, a possible reaction mechanism of the Sn<sub>4</sub>P<sub>3</sub>/C composite as PIB anode is proposed in this paper. This work may open up a new avenue for further development of alloy-based anodes with high capacity and long cycle life for PIBs.

The demand for energy storage materials is high and increasing with the rapid development of electronic devices, electric vehicles, and large-scale energy storage system (ESS).<sup>1-4</sup> The widespread use of lithium-ion batteries (LIBs) for these applications is seriously limited by the uneven distribution and the short supplies of lithium minerals (0.0017 wt. %) around the world.<sup>5</sup> Sodium-ion batteries (SIBs) have recently attracted increasing interest due to the natural abundance of sodium.<sup>6-8</sup> Unfortunately, their relatively high standard hydrogen potential (-2.71 V vs. *E*<sup>o</sup>) compared to LIBs (-3.04 V vs. *E*<sup>o</sup>) makes the energy density of SIBs relatively low and limits their potential industrial applications.<sup>6,9-11</sup>

Considering the similar positions of Li, Na, and K in the periodic table and the natural abundance of potassium<sup>12-16</sup>, the potassium-ion battery (PIB) system could be considered as well. Since the standard hydrogen potential of K (-2.93 V vs. *E*<sup>o</sup>) is lower than that of Na and closer to that of Li, PIBs have potential as low-cost batteries with high energy density and high voltage.<sup>17-20</sup> Nevertheless, it is challenge to develop suitable electrodes to accommodate the large size of the K-ions (1.38 Å) compared to Na-ions and Li-ions. Carbonaceous materials have been investigated as PIB anodes, although the highest reported capacity is 273 mA h g<sup>-1</sup> for soft carbon at C/40.<sup>13</sup>

Although there have been few investigations of alloy-based anode materials in PIBs, an investigation of Sn/C composite anode in a PIB was recently reported, which delivered only 150 mA

h g<sup>-1</sup> after 30 cycles at a current density of 25 mA g<sup>-1</sup>,<sup>21</sup> not much better than for carbon anode materials. Phosphorus (P) has a high theoretical capacity of 2594 mA h g<sup>-1</sup>, since it can form K<sub>3</sub>P, a binary phase with K.<sup>22</sup>

Herein, we have investigated the electrochemical performance of P/C and Sn<sub>4</sub>P<sub>3</sub>/C composites as anode materials for PIBs. The P/C anode delivered a high capacity, but it decayed very fast. In contrast, the Sn<sub>4</sub>P<sub>3</sub>/C electrode delivered a reversible capacity of 384.8 mA h g<sup>-1</sup> at a current density of 50 mA g<sup>-1</sup> and good rate capability of 221.9 mA h g<sup>-1</sup>, even at a current density of 1 A g<sup>-1</sup>, the best electrochemical performance reported so far for any anode material for PIBs. Moreover, the reduction potential of the Sn<sub>4</sub>P<sub>3</sub> electrode in the PIBs was measured to be 0.1 V, higher than its 0.01 V in SIBs. The K-alloy reactions thus occur at a higher potential than the Na-alloy reactions, so that the PIBs with the Sn<sub>4</sub>P<sub>3</sub>/C electrode will have a lower risk of short-circuiting due to dendrite growth.

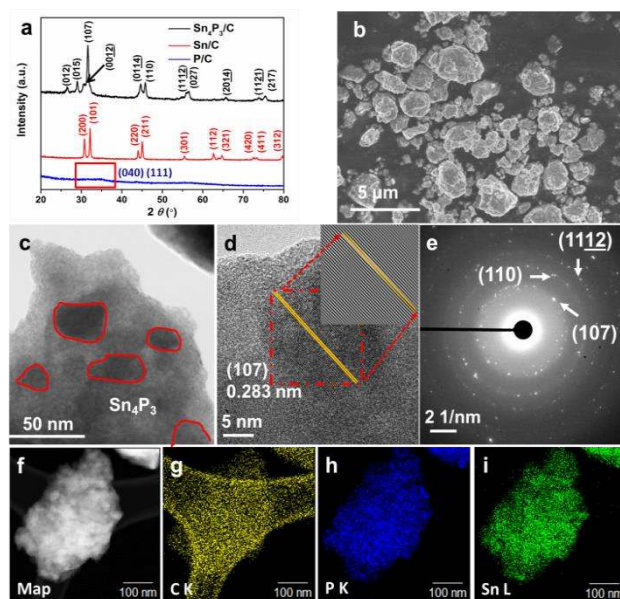


**Figure 1.** Characterization of Sn<sub>4</sub>P<sub>3</sub> powder: a) XRD pattern compared with Sn/C and P/C, b) FESEM image, c) TEM image, with the red outlines indicating the Sn<sub>4</sub>P<sub>3</sub> nanoparticles, d) HRTEM image and FFT pattern of the red area (inset), e) SAED pattern, and f-i) EDS maps of Sn<sub>4</sub>P<sub>3</sub>/C powder.

Figure 1a shows the X-ray diffraction (XRD) patterns of the as-prepared  $\text{Sn}_4\text{P}_3/\text{C}$ ,  $\text{Sn}/\text{C}$ , and  $\text{P}/\text{C}$  powders ball milled under the same conditions. All the diffraction peaks in the XRD pattern of the  $\text{Sn}_4\text{P}_3/\text{C}$  composite and the as-prepared sample is virtually pure  $\text{Sn}_4\text{P}_3$  (ICSD No. 15014). Figures 1b-i display field-emission scanning electron microscopic (FESEM) and transmission electron microscopic (TEM) images of the  $\text{Sn}_4\text{P}_3/\text{C}$  powder. The powder mainly consists of irregular agglomerated micrometre sized particles, as shown in Figure 1b. The agglomerated micro-particles consist of many crystalline nanoparticles around 20-50 nm, distributed evenly in the amorphous carbon matrix (Figure 1c and d). Figure 1d shows the lattice fringes of the (107) planes of  $\text{Sn}_4\text{P}_3$ , and the spacing of the fringes is 0.283 nm, which matches the  $d_{107}$  spacing of  $\text{Sn}_4\text{P}_3$ . The selected area electron diffraction (SAED) pattern and high resolution TEM (HRTEM) image clearly demonstrate that the  $\text{Sn}_4\text{P}_3$  nanoparticles are uniformly distributed in the amorphous carbon matrix, which could act as a buffer to suppress the volume changes during the potassiation/depotassiation. Figure 1f-i presents energy dispersive spectroscopy (EDS) elemental mapping images of a nano- $\text{Sn}_4\text{P}_3$

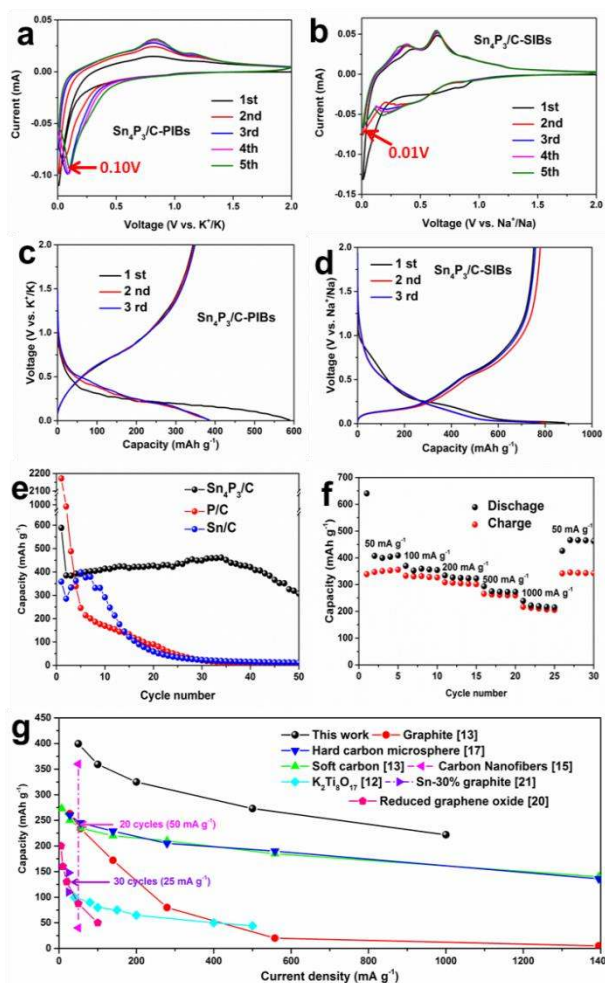


**Figure 2.** Cyclic voltammograms (CVs) for the first 5 cycles of a)  $\text{Sn}_4\text{P}_3/\text{C}$  in PIBs and b)  $\text{Sn}_4\text{P}_3/\text{C}$  in SIBs at the scanning rate of  $0.05 \text{ mV s}^{-1}$ . The initial, second, and third discharge/charge profiles of c)  $\text{Sn}_4\text{P}_3/\text{C}$  in PIBs and d)  $\text{Sn}_4\text{P}_3/\text{C}$  in SIBs at the current density of  $50 \text{ mA g}^{-1}$ . e) Cycling performance of the  $\text{Sn}_4\text{P}_3/\text{C}$ ,  $\text{Sn}/\text{C}$ , and  $\text{P}/\text{C}$  electrodes in PIBs at the current density of  $50 \text{ mA g}^{-1}$ . f) Rate performance of  $\text{Sn}_4\text{P}_3/\text{C}$  electrode in PIBs at various current densities from  $50 \text{ mA g}^{-1}$  to  $1000 \text{ mA g}^{-1}$ . g) Rate capacities of the  $\text{Sn}_4\text{P}_3/\text{C}$  anode and the other reported anodes in PIBs.

particle with uniform distributions of the Sn, P, and C.

The K-ion storage behavior of the  $\text{Sn}_4\text{P}_3/\text{C}$  electrode was investigated by cyclic voltammetry (CV) and compared with its performance in SIBs (Figure 2a and b). For the PIBs (Figure 2a) a major peak at around  $0.01 \text{ V}$  was observed in the initial cathodic scan. During the subsequent cycles, this large reduction band was shifted to  $0.1 \text{ V}$ . In the anodic scan, two oxidation bands centered at  $0.8$  and  $1.15 \text{ V}$  due to the depotassiation processes of  $\text{K-Sn}$  and  $\text{K-P}$  can be observed. The lowest reduction peak for the  $\text{Sn}_4\text{P}_3/\text{C}$  electrode (Figure 2b) is at  $0.1 \text{ V}$  versus  $\text{K}^+/\text{K}$  and  $0.01 \text{ V}$  versus  $\text{Na}^+/\text{Na}$ , respectively. Considering the fact that dendrite formation becomes more serious when the reduction potential is close to the plating potential, PIBs could be safer than SIBs when using  $\text{Sn}_4\text{P}_3$  as anode. The discharge and charge profiles of the  $\text{Sn}_4\text{P}_3/\text{C}$  electrodes for PIBs and SIBs are compared and shown in Figures 2c and d. The discharge slopes for the  $\text{Sn}_4\text{P}_3/\text{C}$  electrode are around  $0.1\text{-}0.6 \text{ V}$  for the PIBs and  $0.01\text{-}0.5 \text{ V}$  for the SIBs, respectively.

Figure 2e displays the cycling performances of the  $\text{Sn}_4\text{P}_3/\text{C}$ ,  $\text{P}/\text{C}$ , and  $\text{Sn}/\text{C}$  electrodes in PIBs at the current density of  $50 \text{ mA g}^{-1}$ . The first discharge capacity of the  $\text{Sn}_4\text{P}_3/\text{C}$  electrode ( $588.7 \text{ mA h g}^{-1}$ ) is higher than that of the  $\text{Sn}/\text{C}$  ( $358.2 \text{ mA h g}^{-1}$ ) but lower than that of the  $\text{P}/\text{C}$  ( $2171.7 \text{ mA h g}^{-1}$ ). The  $\text{P}/\text{C}$  and  $\text{Sn}/\text{C}$  electrodes only managed to retain 9% and 20%, respectively, of their reversible capacity after 20 cycles. In contrast, the  $\text{Sn}_4\text{P}_3/\text{C}$  electrode shows much better cycling performance compared with the  $\text{P}/\text{C}$  and  $\text{Sn}/\text{C}$  electrodes, where the capacity increased gradually up to 30 cycles and faded gradually after that. Nevertheless, the  $\text{Sn}_4\text{P}_3/\text{C}$  electrode still retained the capacity of  $307.2 \text{ mA h g}^{-1}$  after 50 cycles, which is almost 80% of its reversible capacity. Long-term cycling performance was displayed in Fig. S7.

TEM and SEM were carried out on the cycled samples to show the morphology and microstructure changes, as shown in Figures S9 and S10 in the supporting information, respectively. The nano- $\text{Sn}_4\text{P}_3$  particles are still intact in the crystalline state (Fig. S9) but become smaller in size ( $5\text{-}8 \text{ nm}$ ) after 30 cycles. Their even distribution within the carbon matrix provides effective electrode/electrolyte contact, short ionic diffusion paths, and improved reaction kinetics,<sup>23</sup> so that they contribute to the gradual capacity rise before the 30<sup>th</sup> cycle. After the 50<sup>th</sup> cycle, the original crystalline particles were decrystallized and agglomerated into

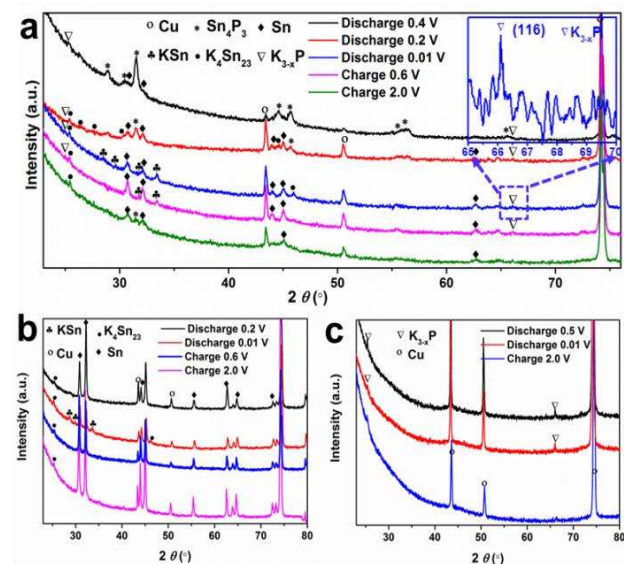
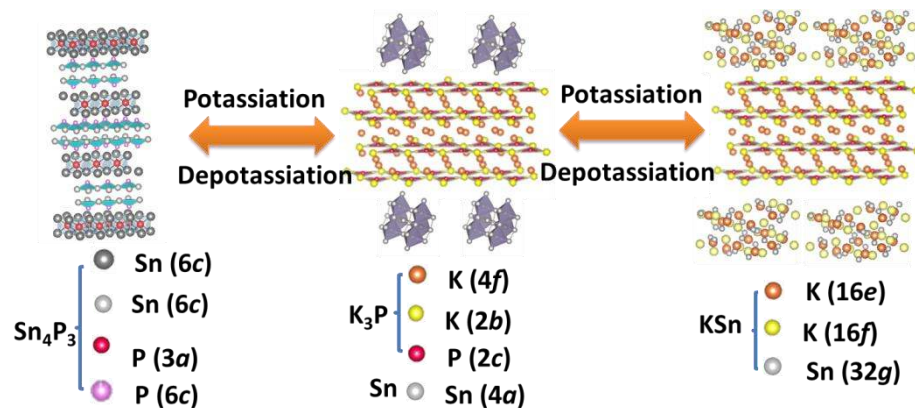


**Figure 3.** Ex-situ XRD patterns of cycled a)  $\text{Sn}_4\text{P}_3/\text{C}$  and enlarged area ( $65^\circ\text{-}70^\circ$ ) at  $0.01 \text{ V}$  at discharged potential (inset), b)  $\text{Sn}/\text{C}$ , and c)  $\text{P}/\text{C}$  electrodes in PIBs at different potentials.





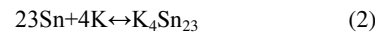
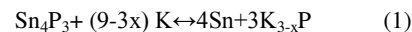
**Scheme 1.** The potassiation/depotassiation process in  $\text{Sn}_4\text{P}_3/\text{C}$  electrode.

larger globules, and the cracks in the  $\text{Sn}_4\text{P}_3/\text{C}$  electrode become much bigger during the cycling process (Fig. S10), mostly after 30 cycles, indicating large strain caused by large volume changes in the  $\text{Sn}_4\text{P}_3$  electrode during cycling, and loss of integrity of the electrode due to particle pulverization leads to decreased capacity.

The rate capability of the  $\text{Sn}_4\text{P}_3/\text{C}$  electrode in PIBs was also characterized, as shown in Figure 2f. The potassiation capacity decreased from 399.4 to 221.9  $\text{mA h g}^{-1}$  when the current density increased from 50  $\text{mA g}^{-1}$  to 1000  $\text{mA g}^{-1}$ . The rate capacities of all the reported anodes used in PIBs (graphite, soft carbon,<sup>13</sup> hard carbon microsphere,<sup>17</sup> carbon nanofibers,<sup>15</sup> Sn/C composite,<sup>21</sup> reduced graphene oxide,<sup>20</sup> and  $\text{K}_2\text{Ti}_8\text{O}_{17}$ <sup>12</sup>) are presented in Figure 2g. It is clear that the rate capability of the  $\text{Sn}_4\text{P}_3/\text{C}$  electrode is the best among the reported anode materials.

To understand the possible reaction mechanisms during the discharge and charge processes, ex-situ XRD was used to identify the possible phases. As shown in Figure 3a, after the  $\text{Sn}_4\text{P}_3/\text{C}$  electrode was discharged to 0.4 V, XRD signals from the  $\text{Sn}_4\text{P}_3$  electrode decreased notably, and XRD signals from  $\text{K}_{3-x}\text{P}$  could be detected. When the  $\text{Sn}_4\text{P}_3/\text{C}$  electrode was further discharged to 0.2 V, Sn phase appeared and became the main phase at the expense of the  $\text{Sn}_4\text{P}_3$ , indicating a conversion reaction. Meanwhile, several new peaks of  $\text{K}_4\text{Sn}_{23}$  (ICSD No. 25301) were observed. After the  $\text{Sn}_4\text{P}_3/\text{C}$  electrode was discharged to 0.01 V, KSn phase (ICSD No. 409435) and minor Sn peaks could be detected, indicating the alloying of potassium with tin. The same results were also obtained in the Sn/C anode, where  $\text{K}_4\text{Sn}_{23}$  and KSn phases were also observed after discharging to 0.2 and 0.01 V, as shown in Figure 3b. It is well known that the binary K-P system has the following phases: KP (ICSD No. 14010),  $\text{K}_4\text{P}_3$  (ICSD No. 64625),  $\text{K}_3\text{P}_{11}$  (ICSD No. 36590), and  $\text{K}_3\text{P}$  (ICSD No. 25550).<sup>22</sup> As for the cycled P/C electrodes, which were discharged to 0.5 or 0.01 V (Figure 3c), two new peaks in addition to the peaks of copper were detected at 25.38° and 65.91°, which correspond to the (102) and (116) of the layered structured  $\text{K}_3\text{P}$  phase with space group  $\text{P6}_3/\text{mmc}$  (Fig. S11). The strongest peak of  $\text{K}_3\text{P}$  is missing, possibly due to partial potassiation, so the final discharge product could be a non-stoichiometric  $\text{K}_{3-x}\text{P}$  compound or amorphous. Based on this discussion, we believe that KSn and  $\text{K}_{3-x}\text{P}$  are the two possible final products after the discharge of the  $\text{Sn}_4\text{P}_3/\text{C}$  electrode in PIBs, with the theoretical capacity of  $\text{Sn}_4\text{P}_3$  as high as 620  $\text{mA h g}^{-1}$ , which is more than 2 times the capacity of carbon anode materials. In the charging process, a new peak at 31.4° was detected after charging to 2.0 V, representing the reformation of the  $\text{Sn}_4\text{P}_3$ . Therefore, the potassiation/depotassiation of  $\text{Sn}_4\text{P}_3$  via conversion and alloying reactions is partially reversible. The reaction mechanism of  $\text{Sn}_4\text{P}_3$  as anode material for SIBs was previously thoroughly investigated,

and in some cases, the  $\text{Sn}_4\text{P}_3$  phase was found to be restored as well, even after desodiation at 1.5 V.<sup>24</sup> Accordingly, the potassiation and depotassiation mechanism may be described by the following equations:



The superior electrochemical performance of the  $\text{Sn}_4\text{P}_3/\text{C}$  composite compared to Sn/C and P/C can be firstly understood from the active nature of the  $\text{Sn}_4\text{P}_3$  itself, where the Sn and P components in the  $\text{Sn}_4\text{P}_3/\text{C}$  are combined to give a synergistic K-storage reaction. The reaction mechanism of  $\text{Sn}_4\text{P}_3$  during potassiation/depotassiation is schematically shown in Scheme 1. Upon potassiation, a conversion reaction first occurs, where the  $\text{Sn}_4\text{P}_3$  breaks into small Sn particles and a  $\text{K}_{3-x}\text{P}$  matrix (Reaction (1)). Upon further potassiation, K is inserted into Sn to first form  $\text{K}_4\text{Sn}_{23}$  (Reaction (2)) and finally KSn (Reaction (3)) through the alloying reaction. During the depotassiation, KSn dealloys first to form Sn, and then the Sn reacts with  $\text{K}_{3-x}\text{P}$  to convert it back to  $\text{Sn}_4\text{P}_3$ . Thus, the stepped formation of K-Sn ( $\text{K}_4\text{Sn}_{23}$ , KSn) and K-P alloy ( $\text{K}_{3-x}\text{P}$ ) phases during the discharge process creates mutual buffers to alleviate the volume changes during cycling. The conductive carbon matrix provides a further buffering effect against volume changes during cycling, thus maintaining the integrity of the electrode and enhancing the electrical conductivity, leading to improved cycling stability of the electrode.

In summary,  $\text{Sn}_4\text{P}_3/\text{C}$  composite, introduced for the first time as an anode material for the potassium-ion battery was synthesised by a conventional and scalable ball-milling technique. Compared with  $\text{Sn}_4\text{P}_3/\text{C}$  in SIBs,  $\text{Sn}_4\text{P}_3/\text{C}$  electrode in PIBs could deliver a discharge voltage plateau (0.1 V) that is low enough for an anode, but slightly higher than the plating potential of the corresponding metal (0.01 V), thus avoiding the formation of dendrites and improving the safety of the battery. Our investigation of the reaction mechanisms of the  $\text{Sn}_4\text{P}_3$  indicates that K-Sn ( $\text{K}_4\text{Sn}_{23}$ , KSn) and K-P alloy ( $\text{K}_{3-x}\text{P}$ ) phases are formed during the discharge process, with these phases acting as mutual buffers to alleviate the volume changes during cycling. The conductive carbon matrix enhances the electrical conductivity of the electrode and works as a buffer matrix to accommodate the volume changes in the active materials during cycling, maintaining the integrity of the electrode and the cycle life. This work may help in the search for a safe, high-energy-density, and low-cost rechargeable K-ion battery for large-scale energy storage applications.

## ASSOCIATED CONTENT

### Supporting Information

The Supporting Information is available free of charge on the ACS Publications website.

Experimental section; additional data from Raman spectroscopy, XPS of  $\text{Sn}_4\text{P}_3/\text{C}$ , SEM, CV curves, discharge-charge profiles of Sn/C and P/C, XRD, Raman and electrochemical results for bare  $\text{Sn}_4\text{P}_3$ , ex-situ TEM and SEM images of  $\text{Sn}_4\text{P}_3/\text{C}$  electrode after cycling, enlarged ex-situ results, ex-situ EDS maps and diffraction patterns, cycling performance with different voltage ranges, crystallography data on  $\text{K}_3\text{P}$  phase.

## AUTHOR INFORMATION

### Corresponding Author

\* [zchen@uow.edu.au](mailto:zchen@uow.edu.au)

\* [zguo@uow.edu.au](mailto:zguo@uow.edu.au)

### Author Contributions

‡These authors contributed equally.

## ORCID

Zaiping Guo: 0000-0003-3464-5301

## Notes

The authors declare no competing financial interests.

## ACKNOWLEDGMENTS

The authors acknowledge the financial support from the Australian Research Council (ARC) through an ARC Discovery Project (DP170102406) and the facilities in the Electron Microscopy Centre of the University of Wollongong (UOW), with special thanks to Dr Wei Kong Pang for the analysis of ex-situ XRD results, Ms. Yajie Liu for Raman tests and Dr Tania Silver for editing. Wenchao Zhang would like to thank the UOW and Engineering Materials Institute of UOW for financial support.

## REFERENCES

- (1) Dubal, D. P.; Ayyad, O.; Ruiz, V.; Gomez-Romero, P. *Chem Soc Rev.* **2015**, *44*, 1777.
- (2) Larcher, D.; Tarascon, J. *Nat Chem.* **2015**, *7*, 19.
- (3) Xie, Y.; Naguib, M.; Mochalin, V. N.; Barsoum, M. W.; Gogotsi, Y.; Yu, X.; Nam, K.-W.; Yang, X.-Q.; Kolesnikov, A. I.; Kent, P. R. *J. Am. Chem. Soc.* **2014**, *136*, 6385.
- (4) Wu, F.; Xing, Y.; Zeng, X.; Yuan, Y.; Zhang, X.; Shahbazian-Yassar, R.; Wen, J.; Miller, D. J.; Li, L.; Chen, R.; Lu, J.; Khalil, A. *Adv Funct Mater.* **2016**, *26*, 7626.
- (5) Goodenough, J. B.; Park, K.-S. *J. Am. Chem. Soc.* **2013**, *135*, 1167.
- (6) Yabuuchi, N.; Kubota, K.; Dahbi, M.; Komaba, S. *Chem. Rev.* **2014**, *114*, 11636.
- (7) Dahbi, M.; Yabuuchi, N.; Kubota, K.; Tokiwa, K.; Komaba, S. *Phys Chem Chem Phys.* **2014**, *16*, 15007.
- (8) Chen, C.; Wen, Y.; Hu, X.; Ji, X.; Yan, M.; Mai, L.; Hu, P.; Shan, B.; Huang, Y. *Nat Commun.* **2015**, *6*.
- (9) Kundu, D.; Talaie, E.; Duffort, V.; Nazar, L. F. *Angew. Chem. Int. Ed. Engl.* **2015**, *54*, 3431.
- (10) Palomares, V.; Casas-Cabanas, M.; Castillo-Martínez, E.; Han, M. H.; Rojo, T. *Energy Environ Sci.* **2013**, *6*, 2312.
- (11) Hong, S. Y.; Kim, Y.; Park, Y.; Choi, A.; Choi, N.-S.; Lee, K. T. *Energy Environ Sci.* **2013**, *6*, 2067.
- (12) Han, J.; Xu, M.; Niu, Y.; Li, G.-N.; Wang, M.; Zhang, Y.; Jia, M.; ming Li, C. *Chem. Commun.* **2016**, *52*, 11274.
- (13) Jian, Z.; Luo, W.; Ji, X. *J. Am. Chem. Soc.* **2015**, *137*, 11566.
- (14) Zhao, Q.; Wang, J.; Lu, Y.; Li, Y.; Liang, G.; Chen, J. *Angew. Chem. Int. Ed. Engl.* **2016**, *128*, 12716.
- (15) Liu, Y.; Fan, F.; Wang, J.; Liu, Y.; Chen, H.; Jungjohann, K. L.; Xu, Y.; Zhu, Y.; Bigio, D.; Zhu, T. *Nano Lett.* **2014**, *14*, 3445.

(16) Wessells, C. D.; Peddada, S. V.; Huggins, R. A.; Cui, Y. *Nano Lett.* **2011**, *11*, 5421.

(17) Jian, Z.; Xing, Z.; Bommier, C.; Li, Z.; Ji, X. *Adv Energy Mater.* **2016**, *6*. doi:10.1002/aenm.201501874.

(18) Eftekhari, A.; Jian, Z.; Ji, X. *ACS Appl Mater Interfaces.* **2016**. doi:10.1021/acsami.6b06767.

(19) Zhao, J.; Zou, X.; Zhu, Y.; Xu, Y.; Wang, C. *Adv Funct Mater.* **2016**. doi:10.1002/adfm.201602248.

(20) Luo, W.; Wan, J.; Ozdemir, B.; Bao, W.; Chen, Y.; Dai, J.; Lin, H.; Xu, Y.; Gu, F.; Barone, V.; Hu, L. *Nano letters* **2015**, *15*, 7671.

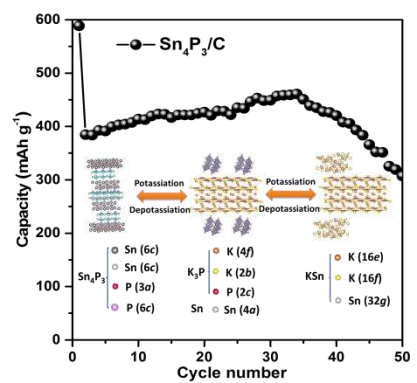
(21) Sultana, I.; Ramireddy, T.; Rahman, M. M.; Chen, Y.; Glushenkov, A. M. *Chem. Commun.* **2016**, *52*, 9279.

(22) Sangster, J. M. *Journal of phase equilibria and diffusion* **2010**, *31*, 68.

(23) Li, X.; Rui, M.; Song, J.; Shen, Z.; Zeng, H. *Adv Funct Mater.* **2015**, *25*, 4929.

(24) Mao, J.; Fan, X.; Luo, C.; Wang, C. *ACS Appl Mater Interfaces.* **2016**, *8*, 7147.

# Table of Contents



# Supporting Information

## Phosphorus-based alloy materials for advanced potassium-ion battery anode

Wenchao Zhang,<sup>a, b, ‡</sup> Jianfeng Mao,<sup>b, ‡</sup> Sean Li,<sup>c</sup> Zhixin Chen,<sup>a, \*</sup> Zaiping Guo<sup>a, b, \*</sup>

<sup>a</sup> Engineering Materials Institute, School of Mechanical, Materials & Mechatronics Engineering, University of Wollongong, NSW 2500, Australia.

<sup>b</sup> Institute for Superconducting & Electronic Materials, University of Wollongong, Wollongong, NSW 2522, Australia.

<sup>c</sup> School of Materials Science and Engineering, The University of New South Wales, NSW 2052, Australia.

\* Corresponding authors: [zchen@uow.edu.au](mailto:zchen@uow.edu.au) (Z. Chen)

[zguo@uow.edu.au](mailto:zguo@uow.edu.au) (Z. Guo)

‡ These authors contributed equally to this work.



## **Experimental Section**

### **Preparation of Sn<sub>4</sub>P<sub>3</sub>/C binary composites**

Sn<sub>4</sub>P<sub>3</sub>/C powder was synthesized by a ball-milling process using elemental Sn (Aldrich,  $\geq 99.8\%$ ), red phosphorus (Aldrich,  $\geq 99\%$ ), and carbon black as the raw materials in the weight ratio of Sn: P: C = 73.1: 14.4: 12.5 (with Sn and P in the molar ratio of 4:3, respectively). The ball milling was conducted in a planetary QM-1SP2 ball mill for 30 h, and the elemental mixture was milled at 500 rpm using stainless steel balls of 10 mm in diameter and with a powder-to-ball weight ratio of 1:30. For comparison, Sn/C and P/C were also synthesized under the same conditions with the weight ratios Sn: C = 87.5: 12.5 and P: C = 87.5: 12.5, respectively. All sample storage and handling were performed in an Ar filled glove box (MBraun Unilab).

### **Materials characterization**

The crystal structures of the as-prepared powders were characterized by powder X-ray diffraction (XRD) on a GBC MMA diffractometer with a Cu K $\alpha$  source at a scanning rate of  $1^\circ \text{ min}^{-1}$ . Raman spectra were collected on a JobinYvon HR800 Raman spectrometer. X-ray photoelectron spectroscopy (XPS) was conducted on a VG Multilab 2000 (VG Inc.) photoelectron spectrometer using monochromatic Al K $\alpha$  radiation under the vacuum of  $2 \times 10^{-6}$  Pa. The morphology of the synthesized powders was characterized on a JEOL JSM-7500FA field-emission scanning electron microscope (FESEM) and a JEOL ARM-200F cold-field-emission and aberration-corrected transmission electron microscope (TEM).

## Electrochemical measurements

Electrodes were fabricated using a slurry-coating method. The synthesized materials ( $\text{Sn}_4\text{P}_3/\text{C}$ ,  $\text{Sn}/\text{C}$ , and  $\text{P}/\text{C}$ ) were mixed with Super P carbon black and carboxymethyl cellulose (CMC) in the weight ratio of 8:1:1, respectively. Deionized (DI) water was used as the dispersing agent. Then, the slurry was coated on copper foil and dried in a vacuum oven at 80 °C overnight. Coin-type (CR2032) cells were assembled in an argon-filled glove box with oxygen and water content lower than 0.1 ppm. K half-cells were assembled with potassium metal and 0.8 M  $\text{KPF}_6$  in an ethylene carbonate (EC) – diethyl carbonate (DEC) solution (EC: DEC = 1:1) as electrolyte. Na half-cells were assembled with sodium metal and 0.8 M  $\text{NaPF}_6$  in EC-DEC solution (EC: DEC = 1:1) as electrolyte. The mass loading of active material ( $\text{Sn}_4\text{P}_3$ ) was over  $0.78 \text{ mg cm}^{-2}$ , corresponding to a total mass loading of  $1.11 \text{ mg cm}^{-2}$ . Cyclic voltammetry (CV) tests were conducted on a VMP-3 electrochemical workstation at a scan rate of  $0.05 \text{ mV s}^{-1}$ . The cells were galvanostatically charged-discharged between 0.01 and 2.0 V versus  $\text{K}/\text{K}^+$  or  $\text{Na}/\text{Na}^+$  at various current densities on a Land battery tester. The specific capacity was calculated based on the weight of  $\text{Sn}_4\text{P}_3$ . The mass loading of active material was increased to over  $1.7 \text{ mg cm}^{-2}$  for ex-situ XRD experiments.

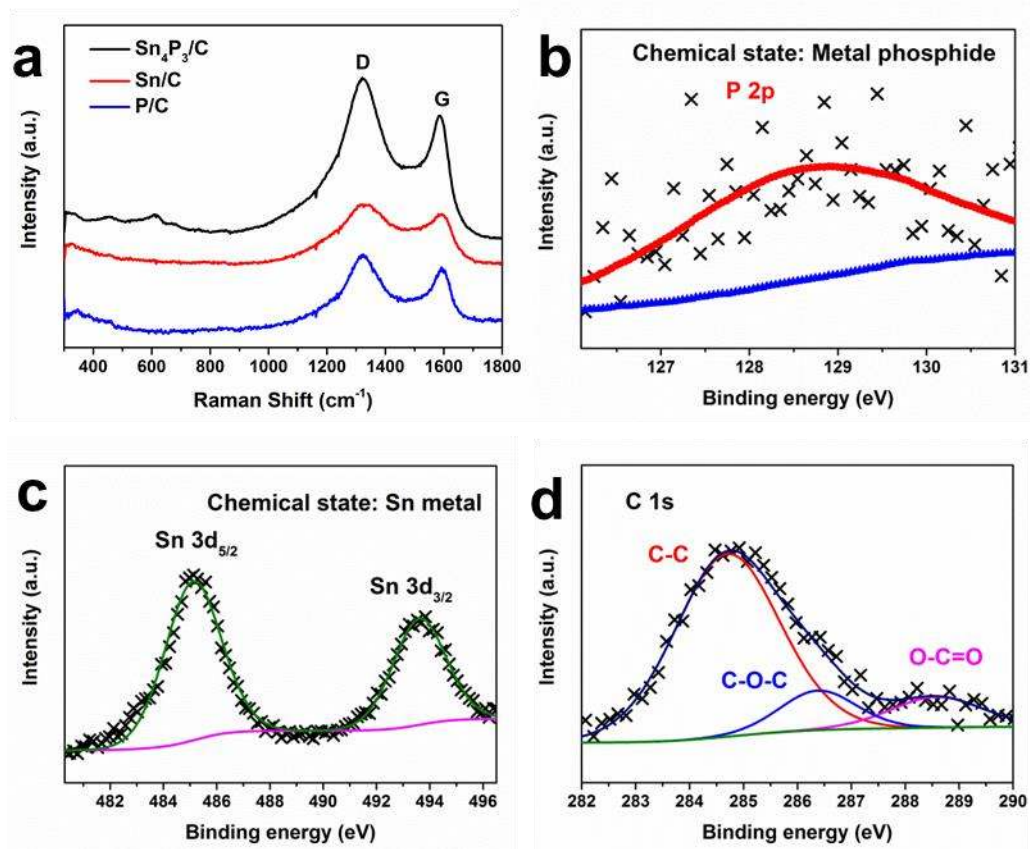


**Figure S1.** a) Raman spectra of the as-prepared Sn<sub>4</sub>P<sub>3</sub>/C, Sn/C, and P/C powders. XPS analysis of b) P 2p, c) Sn 3d, and d) C 1s peaks from Sn<sub>4</sub>P<sub>3</sub>/C powder.

Raman spectroscopy was used to identify the carbon black in the three samples, as shown in Figure S1a. The two peaks at 1355 cm<sup>-1</sup> and 1580 cm<sup>-1</sup> correspond to the disordered (D) band and the graphitic (G) band of carbon black, respectively. The X-ray photoelectron spectroscopy (XPS) results for the Sn<sub>4</sub>P<sub>3</sub>/C composite are presented in Figure S1b-d and they show a metallic feature (Sn) and metal phosphide for the P component. This explains the high electrical conductivity of Sn<sub>4</sub>P<sub>3</sub> (30.7 S cm<sup>-1</sup> for Sn<sub>4</sub>P<sub>3</sub> vs.  $3.5 \times 10^{-5}$  S cm<sup>-1</sup> for P/C composite).<sup>1,2</sup> No chemical bonding between carbon and P or Sn is evidenced by the XPS results.

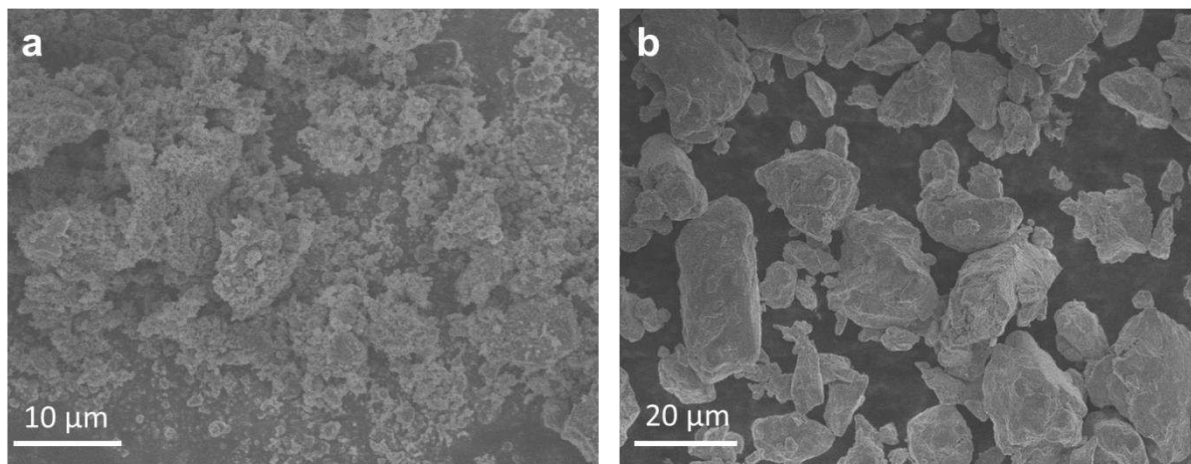


**Figure S2.** SEM images of a) P/C, b) Sn/C powders.

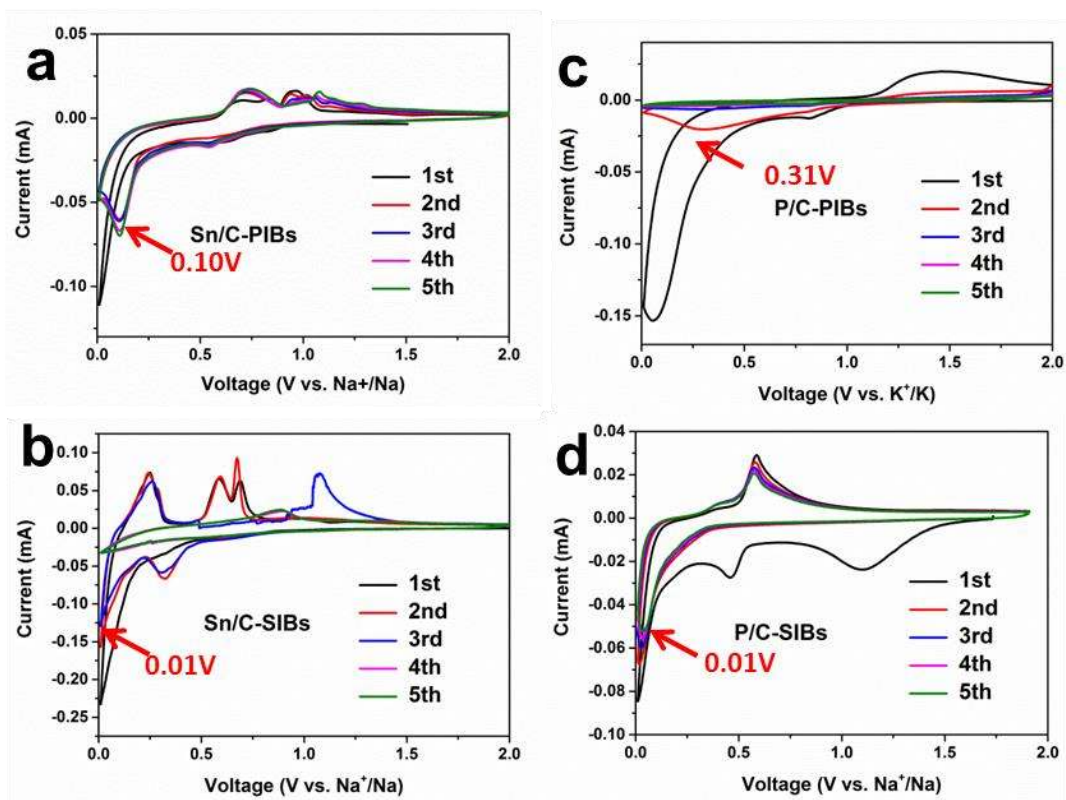


**Figure S3.** CV curves for the first 5 cycles at the scanning rate of  $0.05 \text{ mV s}^{-1}$  for a) Sn/C in PIBs, b) Sn/C in SIBs, c) P/C in PIBs, and d) P/C in SIBs.



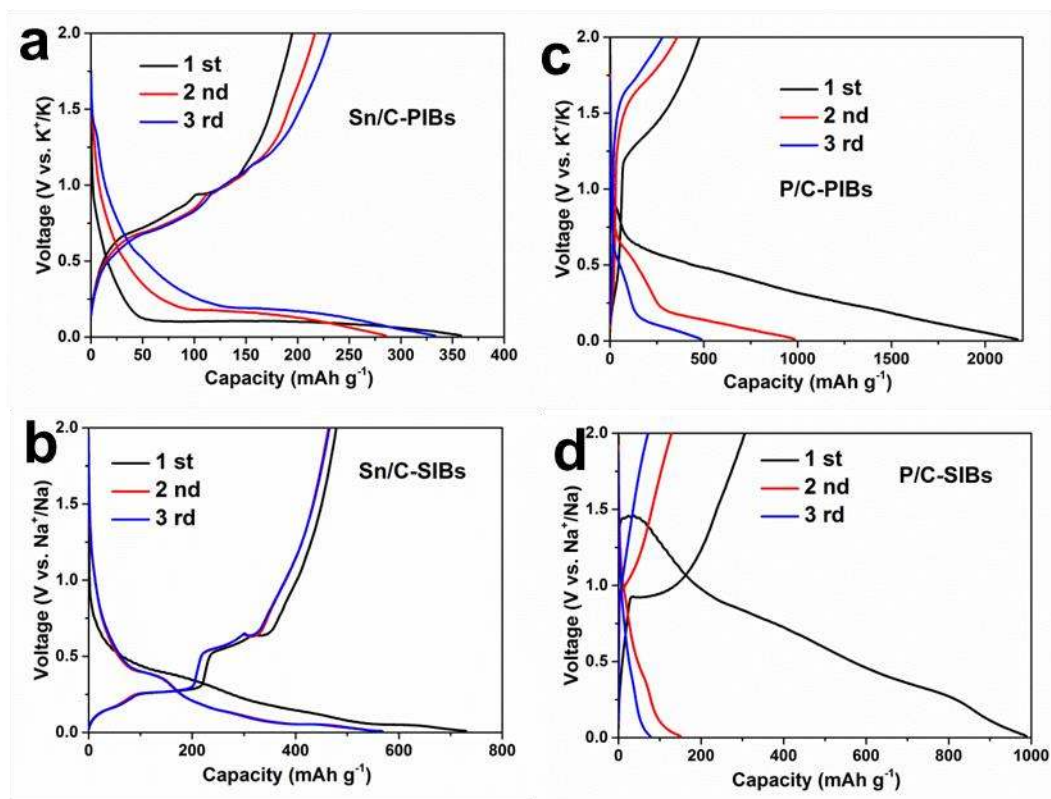


**Figure S4.** Discharge/charge profiles for the first 3 cycles of a) Sn/C in PIBs, b) Sn/C in SIBs, c) P/C in PIBs, and d) P/C in SIBs at the current density of 50 mA g<sup>-1</sup>.

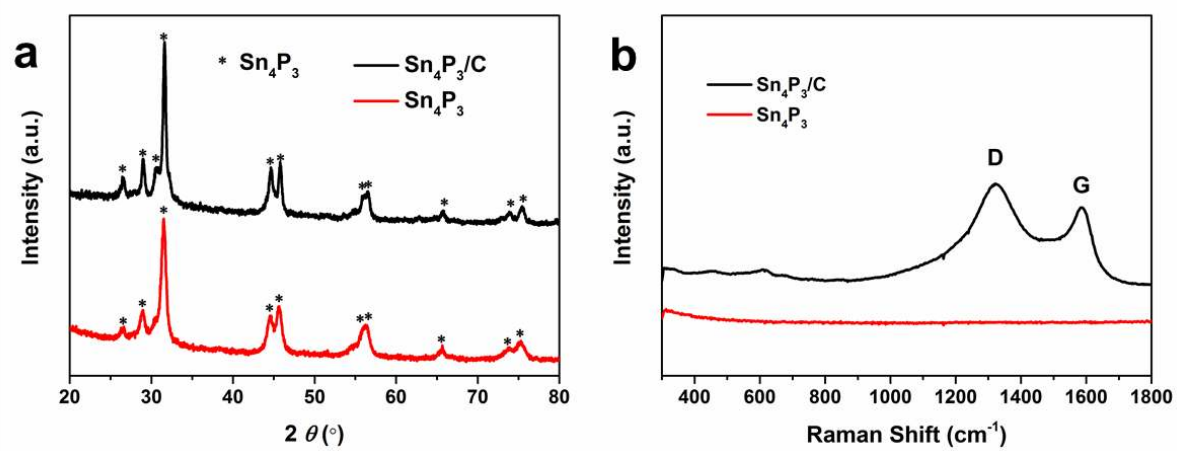


**Figure S5.** a) XRD patterns and b) Raman spectra of the as-prepared  $\text{Sn}_4\text{P}_3/\text{C}$  and  $\text{Sn}_4\text{P}_3$  powders.

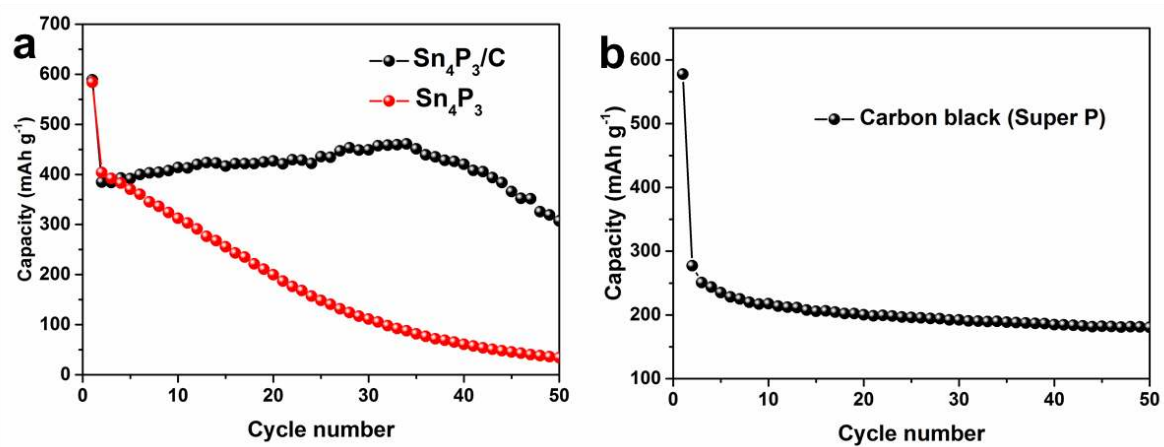


**Figure S6.** Cycling performance of a) Sn<sub>4</sub>P<sub>3</sub>/C and Sn<sub>4</sub>P<sub>3</sub> electrodes, and b) carbon black (Super P) electrode.

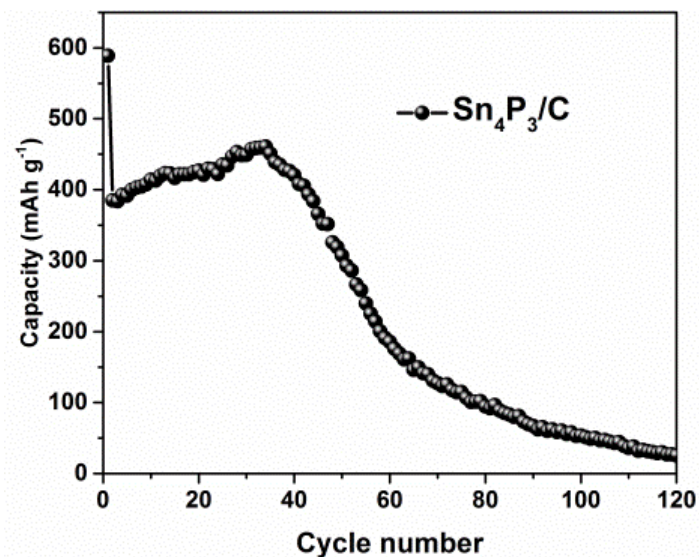


**Figure S7.** Long-term cycling performance of the  $\text{Sn}_4\text{P}_3/\text{C}$  electrode in PIBs at the current density of  $50 \text{ mA g}^{-1}$ .

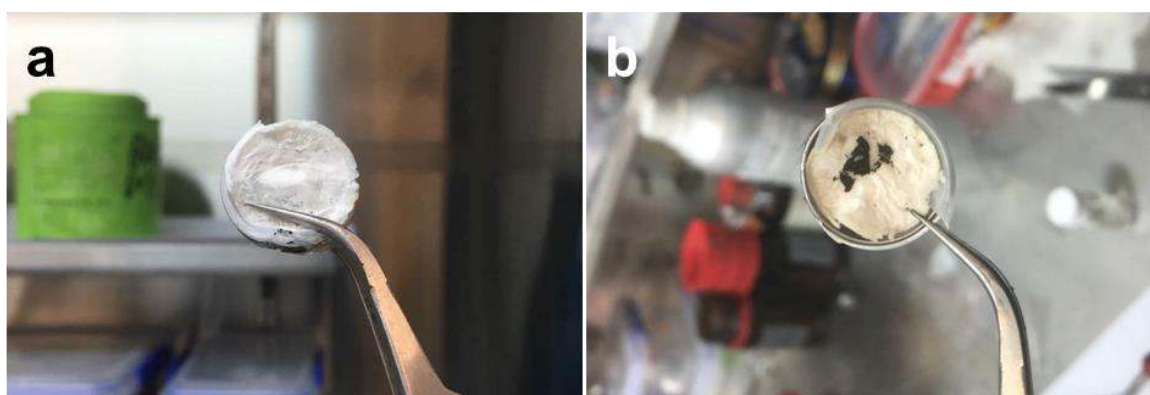


**Figure S8.** Digital photographs of separator after c) the 1<sup>st</sup> cycle and d) the 50<sup>th</sup> cycle.

The long-term cycling performance of the  $\text{Sn}_4\text{P}_3/\text{C}$  electrode for PIBs is shown in Fig. S7. After 50 cycles, the capacity of the  $\text{Sn}_4\text{P}_3/\text{C}$  decreases very rapidly. The fast capacity drop is mainly due to the large particle size and the non-uniform distribution of  $\text{Sn}_4\text{P}_3$  particles in the carbon black due to the limitations of the ball-milling technique. Figure S8a and S8b present digital photographs of separators after the 1<sup>st</sup> cycle and the 50<sup>th</sup> cycle. After 50 cycles, many particles have fallen off the copper foil, which will cause a huge loss of active materials and carbon, as well as leading to capacity loss.

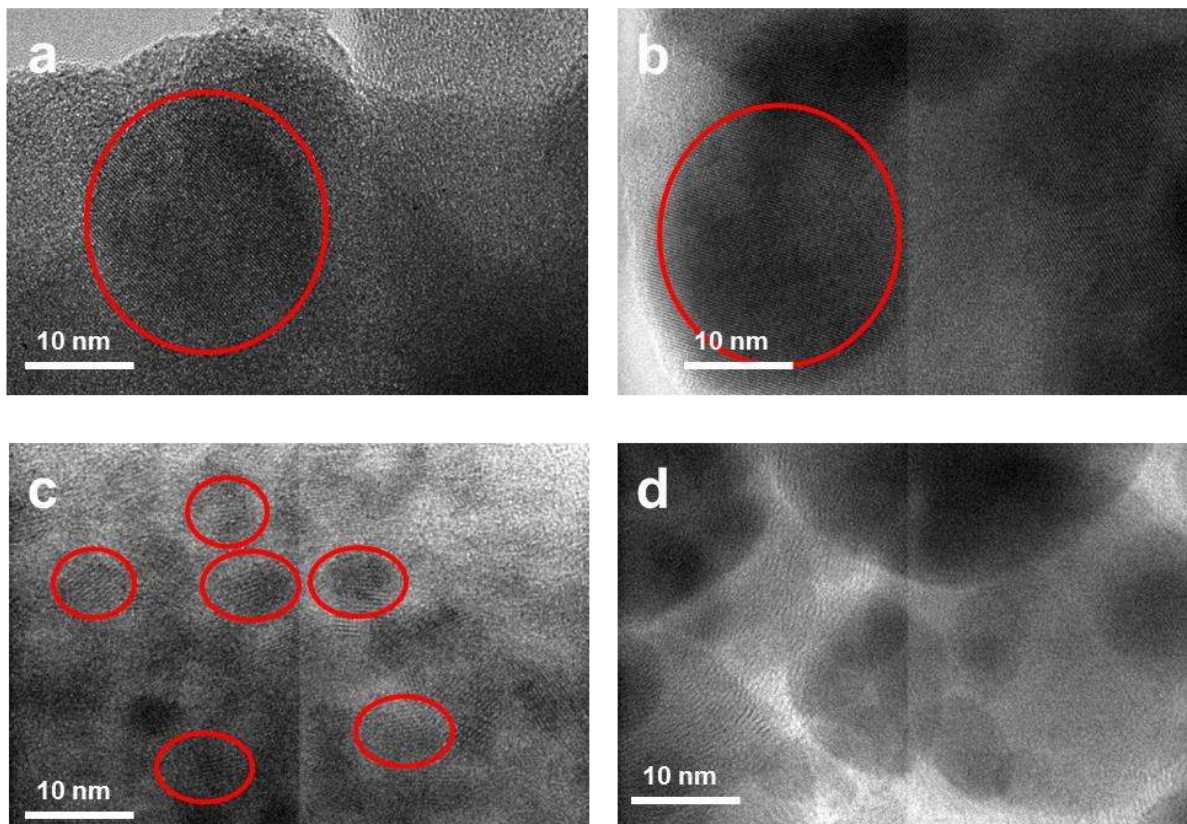


**Figure S9.** Ex-situ TEM images of  $\text{Sn}_4\text{P}_3/\text{C}$  electrodes: a) pristine, and after b) the 10<sup>th</sup> cycle, c) the 30<sup>th</sup> cycle, and d) the 50<sup>th</sup> cycle. The red circles identify the  $\text{Sn}_4\text{P}_3$  nanoparticles in the carbon matrix.



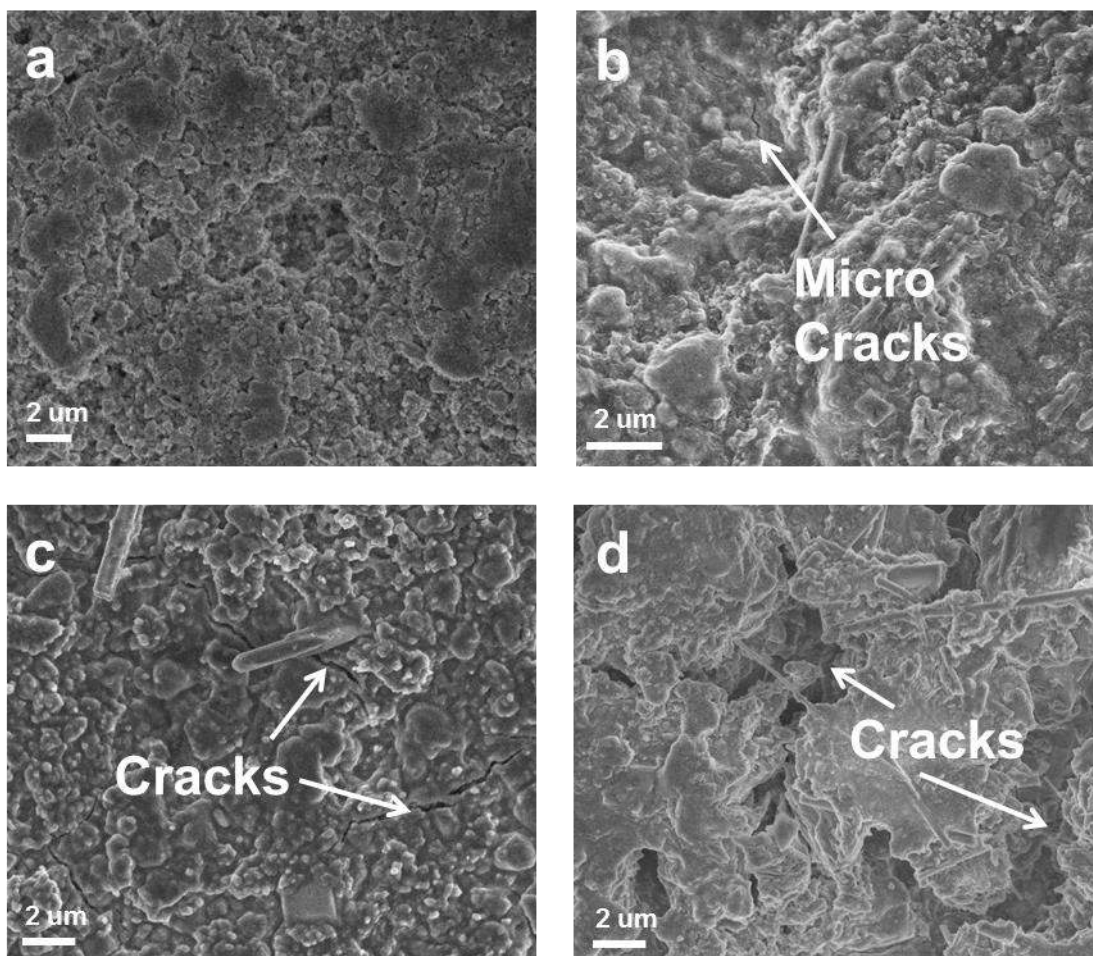


**Figure S10.** Ex-situ FESEM images of Sn<sub>4</sub>P<sub>3</sub>/C electrodes: a) pristine, and after b) the 10<sup>th</sup> cycle, c) the 30<sup>th</sup> cycle, and d) the 50<sup>th</sup> cycle.

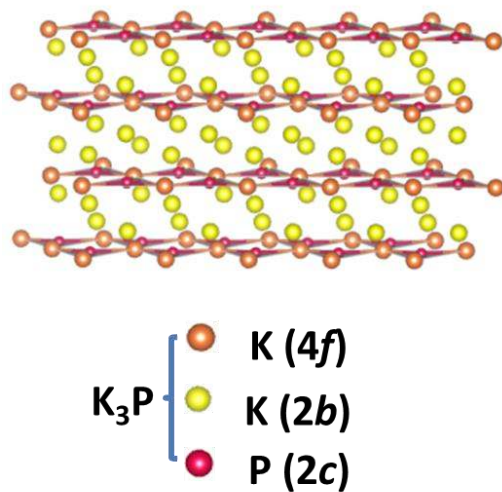


**Figure S11.** Schematic diagrams of the crystal structure of  $K_3P$

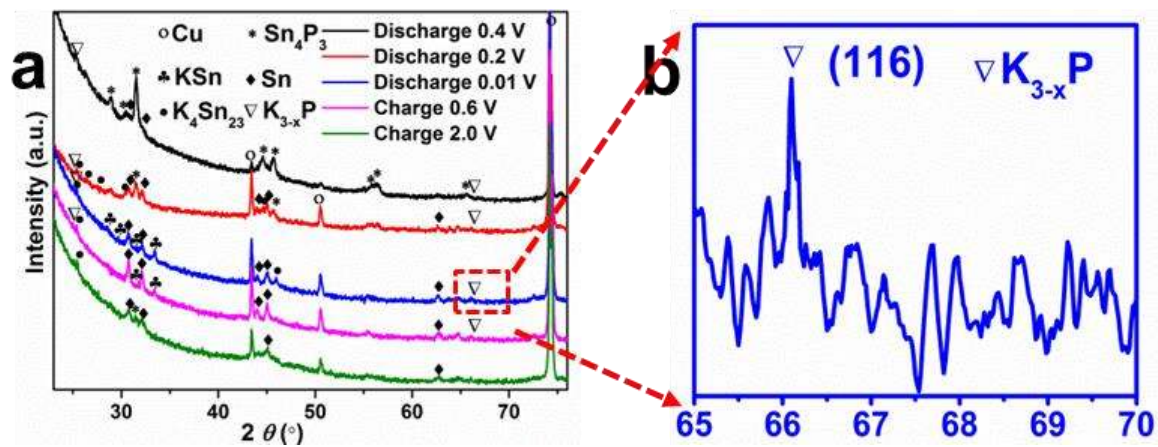


**Figure S12.** a) Ex-situ XRD patterns of cycled  $\text{Sn}_4\text{P}_3/\text{C}$  electrode in PIBs at different potentials, and b) enlarged area ( $65^\circ$ - $70^\circ$ ) at 0.01 V discharge potential.

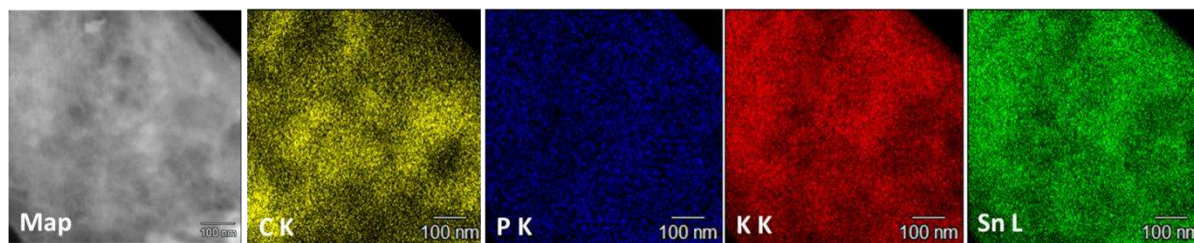


**Figure S13.** EDS maps of cycled  $\text{Sn}_4\text{P}_3/\text{C}$  electrode after it was discharged to 0.01 V.

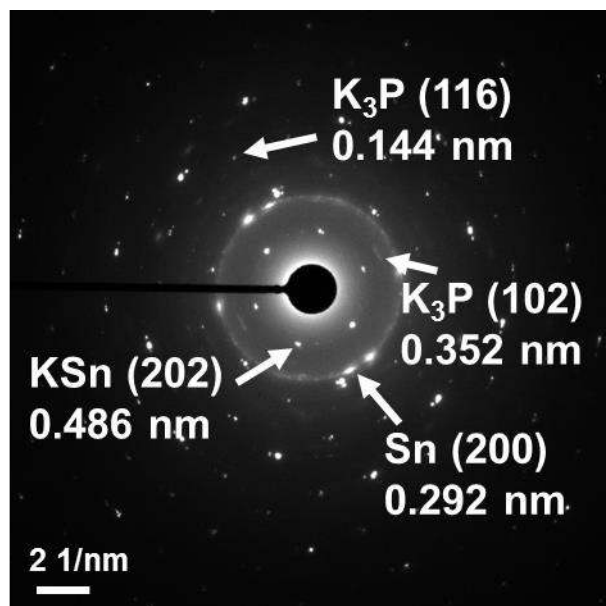


**Figure S14.** SAED pattern of cycled  $\text{Sn}_4\text{P}_3/\text{C}$  electrode after it was discharged to 0.01 V.

Figure S13 presents energy dispersive spectroscopy (EDS) elemental mapping images of a cycled  $\text{Sn}_4\text{P}_3/\text{C}$  electrode with uniform distributions of the Sn, P, C, and K. Figure S14 shows the selected area electron diffraction (SAED) pattern of cycled  $\text{Sn}_4\text{P}_3/\text{C}$  electrode. The  $d$ -spacings of the diffraction rings can be measured as 0.486, 0.352, 0.292 and 0.144 nm, which correspond to (202) of KSn, (102) of  $\text{K}_3\text{P}$ , (200) of Sn, and (116) of  $\text{K}_3\text{P}$ , respectively, which is consistent with the XRD results.

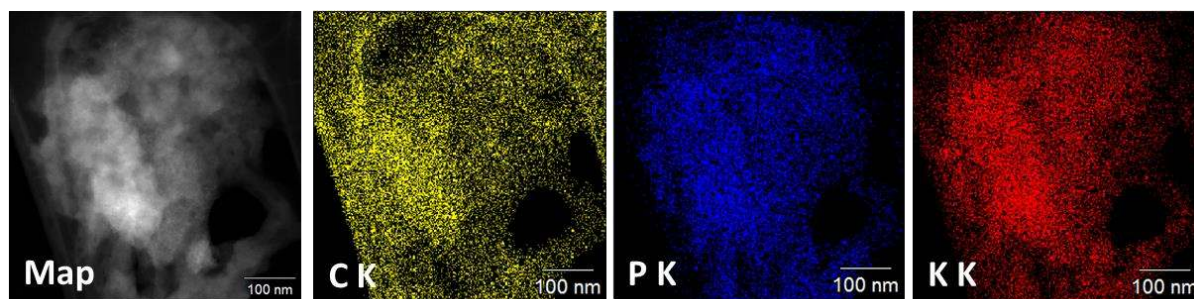


**Figure S15.** EDS maps of cycled P/C electrode after it was discharged to 0.01 V.

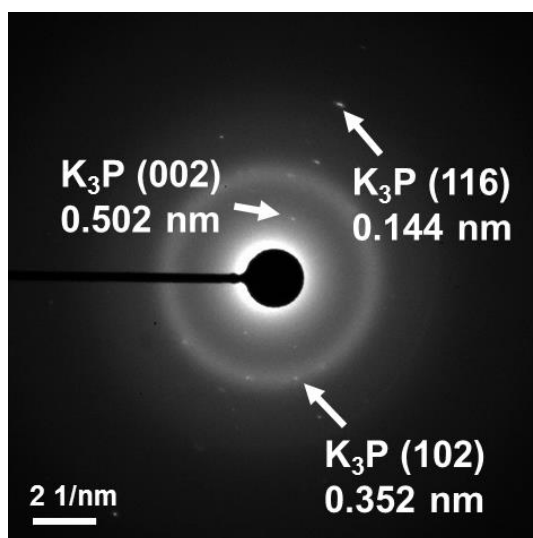


**Figure S16.** SAED pattern of cycled P/C electrode after it was discharged to 0.01 V.

Similar  $d$ -spacing of diffraction rings from  $K_3P$  was also observed in the SAED pattern of a cycled P/C electrode, further confirming the existence of  $K_3P$  in the cycled  $Sn_4P_3/C$  electrode after potassiation. Figure S16 shows the selected area electron diffraction (SAED) pattern of the cycled P/C electrode. The  $d$ -spacings of the diffraction rings can be measured as 0.502, 0.352 and 0.144 nm, corresponding to (002), (102), and (116) of  $K_3P$ , respectively. The diffuse diffraction ring is due to the carbon in the composite and the supporting carbon film.



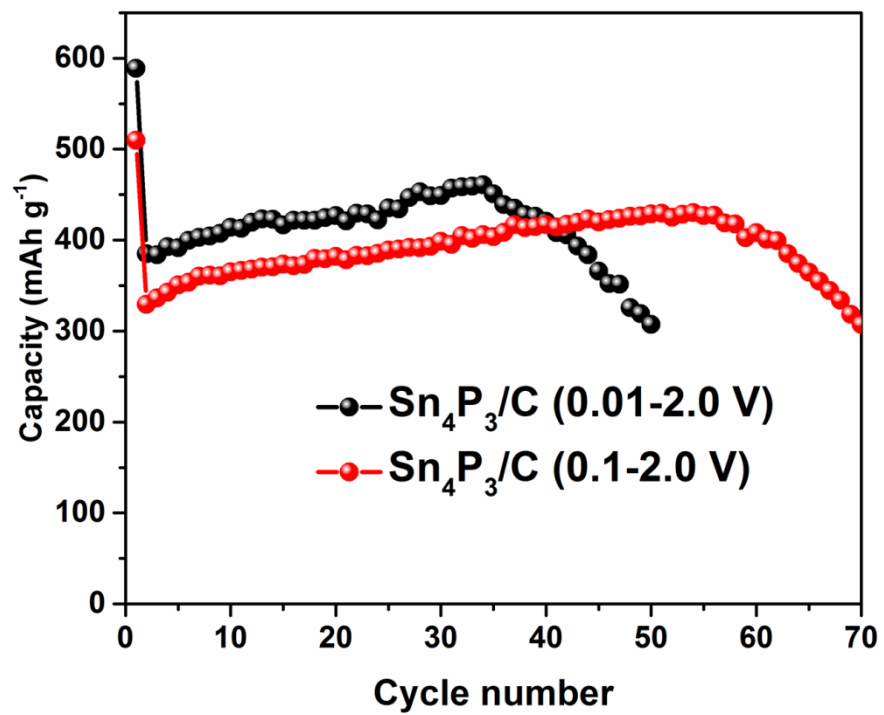


**Figure S17.** Cycling performance of the  $\text{Sn}_4\text{P}_3/\text{C}$  electrode in PIBs in the voltage range of 0.1-2 V (compared with 0.01-2 V)

**Table S1** Crystallography data on K<sub>3</sub>P phase

| Space group          | Lattice parameters |         |         |          |         |          | Unit-cell volume (Å <sup>3</sup> ) | Bond length               | Interlayer distance |
|----------------------|--------------------|---------|---------|----------|---------|----------|------------------------------------|---------------------------|---------------------|
|                      | a                  | b       | c       | $\alpha$ | $\beta$ | $\gamma$ |                                    |                           |                     |
| P6 <sub>3</sub> /mmc | 5.691 Å            | 5.691 Å | 10.05 Å | 90°      | 90°     | 120°     | 281.886                            | K(2b)-P(2c)::<br>3.2857 Å | 5.025 Å             |

## REFERENCES

- (1) Liu, J.; Kopold, P.; Wu, C.; van Aken, P. A.; Maier, J.; Yu, Y. *Energy Environ Sci.* **2015**, *8*, 3531.
- (2) Kim, Y.; Park, Y.; Choi, A.; Choi, N. S.; Kim, J.; Lee, J.; Ryu, J. H.; Oh, S. M.; Lee, K. T. *Adv Mater.* **2013**, *25*, 3045.